Enclosure

1. **Q. Yue**, J. Zhang, M. Shamzhy, M. Opanasenko*. Seeded growth of isomorphously substituted chabazites in proton-form. **Microporous Mesoporous Mater.** 2019, 280, 331-336.

2. V. Kasneryk, M. Shamzhy, J. Zhou, **Q. Yue**, M. Mazur, A. Mayoral, Z. Luo*, R. E. Morris, J. Čejka, M. Opanasenko*. Vapour-phase-transport rearrangement technique for the synthesis of new zeolites. **Nat. Commun.** 2019, 10, 5129.

Declaration of Authorship

I declare that I have presented this dissertation independently and I have properly cited all literatures. This work has not been submitted to obtain any other academic degree.

The dissertation was completed based on the following publications

1. **Q. Yue**, J. Zhang, M. Shamzhy, M. Opanasenko*. Seeded growth of isomorphously substituted chabazites in proton-form. **Microporous Mesoporous Mater.** 2019, 280, 331-336.

2. V. Kasneryk, M. Shamzhy, J. Zhou, **Q. Yue**, M. Mazur, A. Mayoral, Z. Luo*, R. E. Morris, J. Čejka, M. Opanasenko*. Vapour-phase-transport rearrangement technique for the synthesis of new zeolites. **Nat. Commun.** 2019, 10, 5129.

My contributions to these publications were as follows:

In the 1st paper, I optimized the synthesis conditions for CHA zeolites and conducted the synthesis experiments. I performed XRD, SEM characterizations. I participated in data analysis, manuscript writing and addressing the reviewer's comments. My overall contribution is 80 %.

In the 2nd paper, I performed lab-scale optimisation of the synthesis and basic characterisation of materials. I participated in the *in-situ* XRD experiments analysis, manuscript editting. My overall contribution is 35 %.

Signature: **Supervisor**:

Date: 31.05.2021

Microporous and Mesoporous Materials 280 (2019) 331–336

Contents lists available at ScienceDirect

Microporous and Mesoporous Materials

journal homepage: www.elsevier.com/locate/micromeso

Seeded growth of isomorphously substituted chabazites in proton-form

Qiudi Yue, Jin Zhang, Mariya Shamzhy, Maksym Opanasenko*

Department of Physical and Macromolecular Chemistry, Faculty of Science, Charles University, Hlavova 2030/8, 128 40, Prague 2, Czech Republic

ARTICLE INFO

Keywords:
Zeolites
Chabazite
Isomorphous substitution
Crystal seeds

ABSTRACT

Isomorphous substitution of 3- and 4-valent heteroelements for Si is a practical approach to develop a zeolite catalyst with high activity and selectivity. Different nature of incorporated heteroatoms within the framework of the host zeolites makes the crystallization process challenging and time-consuming. Herein, we developed a practical approach to synthesize a set of heteroelement-substituted chabazites in proton form (M-CHA[H], M = B, Al, Ga, and Ti) using the pure silica CHA (Si-CHA) as the crystal growth seeds. The time required to obtain highly crystalline M-CHA[H] was significantly reduced in comparison with existing procedures. The incorporated heteroatoms were proved to be located in the framework of CHA using FTIR and UV–Vis spectroscopy. Thus, the proposed approach has been demonstrated as a facile and fast way to synthesize the isomorphously substituted CHA in proton form.

1. Introduction

Zeolites, being characteristic of a unique combination of chemical flexibility with high porosity, have been widely utilized in catalytic processes, ion exchange, and gas separation [1,2]. Diversification of the framework elements of zeolites can provide materials with specific functionality for particular applications [3,4]. The isomorphous substitution of Si for other tetrahedrally coordinated heteroatoms, such as B^{III}, Al^{III}, Ti^{IV}, Ga^{III} and Fe^{III}, can substantially alter the physicochemical properties of the materials and also provide materials with active sites for specific catalytic properties [5]. Since the acid strength depends on the nature of incorporated heteroelement, isomorphous incorporation of different heteroelements into the zeolites has also been extensively studied [6,7].

Two general methods, post-synthesis using wet-impregnation [8] and direct synthesis [9,10], are utilized for the synthesis of heteroatom-incorporated zeolites. Typically, heteroatoms introduced by a post-synthesis are unevenly distributed that results in formation of heteroatom-enriched domains within the framework preferentially located close to the surface of zeolites. Moreover, formation of extra-framework deposits can result in channel blocking and decreasing the accessibility of catalytically active sites [11]. In contrast, direct synthesis by the conventional hydrothermal method is well adopted for design of materials with uniform distribution of the heteroelements in the framework [12]. The synthesis process is often realized in the alkaline media in the presence of alkali metal cations [13]. As a result, as-prepared zeolites need additional multistep ion-exchange and calcination processes to transfer it to proton form required for the most of catalytic applications involving zeolites. Therefore, the direct synthesis of isomorphously substituted zeolites in proton form is preferred.

Chabazite with **CHA** topology, a representative small-pore zeolite, has attracted particular attention because it has 3-dimensional structure with 8-rings and intersecting channels with a diameter of 3.8 Å. Chabazite zeolite have been demonstrated as a good deNOx catalyst when ion exchanged with copper [11,14,15]. SAPO-34 zeolite with **CHA** topology has been proven to be the best catalyst for the production of ethylene and propylene in the methanol-to-olefin (MTO) reaction [16–18]. Furthermore, chabazite contains only one crystallographic independent T site and is, therefore, an interesting model material to study heteroelements insertion in the framework [19–21]. Many publications demonstrated that the isomorphously substituted **CHA** exhibit specific shape selectivity for the conversion of methanol into light olefins depending on the heteroelement nature [22–24]. However, the direct synthesis methods towards isomorphously substituted **CHA** are still challenging and time-consuming because of slow crystallization kinetics. Theoretical studies have shown that the substitution energy necessary for the synthesis of proton form **CHA** (CHA[H]) is much higher than cationic form **CHA** (Li, Na, K, and NH_4) [25]. For boron-substituted CHA[H] (B-CHA[H]), the absolute substitution energy is positive, making this synthesis thermodynamically unfavorable. As a result, Lin et al. reported that B-CHA[H] can be obtained in 15 days with good crystallinity in a direct synthesis [26]. Several approaches have been attempted to accelerate the crystallization such as the use of microwave radiation [27] and UV irradiation [28]. Recently, seeding

* Corresponding author.
E-mail address: maksym.opanasenko@jh-inst.cas.cz (M. Opanasenko).

https://doi.org/10.1016/j.micromeso.2019.02.017
Received 17 December 2018; Received in revised form 4 February 2019; Accepted 12 February 2019
Available online 13 February 2019
1387-1811/ © 2019 Elsevier Inc. All rights reserved.

method has been demonstrated to be a facile way to direct the growth of targeted crystals and also to shorten the synthesis time [29–31]. Up to now, however, there is no report in the literature dedicated to the direct one-step synthesis of isomorphously substituted CHA[H] zeolites with the aid of seeds.

This contribution focuses on the development of a direct one-step synthesis of isomorphously substituted CHA[H] zeolites. Pure silica Si-CHA crystals were synthesized and then submitted as the seeds to direct the growth of heteroelements substituted M-CHA[H] (M = B, Al, Ga, and Ti) to reduce the time of the synthesis of heteroelements substituted CHA[H] in comparison with the previous reports. The influences of the nature of heteroelements on the textural characteristics (the size and shape of the crystal, porosity) and acidic properties of the M-CHA[H] are carefully addressed.

2. Experimental

N,N,N-trimethyl-1-adamantane ammonium iodide (TMAdaI) used as the structural directing agent (SDA) was synthesized according to the previous report [13]. N,N,N-trimethyl-1-adamantane ammonium hydroxide (TMAdaOH) was obtained by ion exchange using hydroxide ion exchange resin(Ambersep 900(OH)).

2.1. Synthesis of Si-CHA

Pure Si-CHA zeolite was synthesized according to Ref. [32] from reaction mixture with the following composition: 1 SiO_2: 0.5 TMAdaOH: 0.5 HF: $3H_2O$, at 433 K for 48 h. The as-prepared Si-CHA was calcined at 600 °C for 6 h at a ramp rate of 1 °C min^{-1} to remove the SDA. The calcined Si-CHA was used as the seed to direct the growth of Al-CHA[H], B-CHA[H], Ti-CHA[H], and Ga-CHA[H] crystals.

2.2. Synthesis of Al-CHA[H], B-CHA[H], and Ga-CHA[H] zeolites

For the synthesis of Al-CHA[H], B-CHA[H], and Ga-CHA[H], $Al(OH)_3$, H_3BO_3, and $Ga(NO_3)_3{\cdot}xH_2O$ were used as Al, B, and Ga sources, respectively. The initial gel composition was set as 1 SiO_2: x TMAdaOH: y Al (or B, Ga): $44H_2O$, x = 0.5 for Al-CHA[H], 0.4 for B-CHA[H] and Ga-CHA[H], and y = 0.05, 0.2, and 0.05 for Al-CHA[H], B-CHA[H], and Ga-CHA[H], respectively. Typically, 40 mg $Al(OH)_3$ was dissolved in the TMAdaOH solution, then 1.5 g colloidal silica (40 wt%) was added into the solution under stirring at room temperature for 2 h. When the gel reached to the desired composition, then, 12 mg (2 wt%) Si-CHA was added into the gel. The desired gel was transferred to a Teflon container, charged into an autoclave, and then hydrothermally treated at 150 °C for 1 day. After the reaction, the autoclave was cooled down under the flowing water. The product was washed out with distilled water and ethanol and recovered by centrifugation. For the synthesis of B-CHA[H] and Ga-CHA[H], colloidal silica was replaced by fumed silica as the Si source, and the gels were crystallized for 1 day and 3 days, respectively. The obtained solid was dried at room temperature, and then calcined in air at 600 °C (ramp rate of 1 °C min^{-1}) to remove the SDA.

2.3. Synthesis of Ti-CHA[H] zeolite

Ti-CHA[H] was synthesized in the same way as the Al-CHA[H] from a gel composition of 1 SiO_2: 0.05 TiO_2: 1.4 TMAdaOH: 1.4 HF: $6H_2O$. First, titanium ethoxide was added into the TMAdaOH solution and stirred for 20 min. Then, 1.5 g colloidal silica was added and stirred under room temperature for overnight. After that, HF (40 wt%) was added. After reaching the final gel composition, 2 wt% Si-CHA was added into the gel, and then the gel was transferred to a Teflon container, charged into an autoclave, and then hydrothermally treated at 150 °C for 30 h. The later washing and calcination process of the products is the same with other M-CHA[H].

2.4. Characterization

The crystallinity of all samples under investigation was determined by XRD by using a Bruker AXS-D8 Advance diffractometer with a graphite monochromator using Cu Kα radiation in Bragg–Brentano geometry. The morphologies of copper-coated samples were determined by scanning electron microscope a TESCAN Vega. Nitrogen adsorption/desorption isotherms were measured using an ASAP 2020 (Micromeritics) static volumetric apparatus at −195.79 °C. Prior to the sorption measurements, all samples were degassed with a turbo molecular pump at 250 °C for 4 h. The Brunauer–Emmett–Teller (BET) equation was used to calculate the apparent surface area from the adsorption data obtained at P/P_0 between 0.05 and 0.2. P, pressure; P_0, standard pressure. The chemical species of Ti in the framework of the Ti-CHA[H] zeolite were analyzed by UV–Vis spectroscopy (Fluorolog®-3, Horiba). The chemical composition was determined by the Inductively coupled plasma - optical emission spectrometry (ICP-OES, Thermo Scientific iCAP 7000).

The concentration of Lewis and Brønsted acid sites (LAS and BAS) was determined by FTIR spectroscopy of adsorbed d_3-acetonitrile (AN) using a Nicolet iS50 spectrometer with a transmission MTC/B detector. FTIR spectra in the framework region were recorded in ATR mode using Nicolet iS50 spectrometer equipped with a single reflection diamond ATR module and a DTGS detector, working with a spectral resolution of 4 cm^{-1}. The zeolites were pressed into self-supporting wafers with a density of ~10 mg cm^{-2} and activated in situ at T = 450 °C and p = 5×10^{-5} Torr for 4 h. All spectra were recorded with a resolution of 4 cm^{-1} by collecting 128 scans for a single spectrum at room temperature. Spectra were recalculated using a wafer density of 10 mg cm^{-2}. Concentrations of LAS and BAS in T^{III}-CHA[H] were evaluated from the integral intensities of bands at 2323 cm^{-1} (strong LAS), 2310 cm^{-1} (weak LAS) and at 2294 cm^{-1} (BAS) using molar absorption coefficients, ε(LAS) = 3.6 cm μmol^{-1}, and ε(BAS) = 2.05 cm μmol^{-1} [33]. AN adsorption in Si-, B-, Al-, Ga-CHA[H] was carried out at 25 °C for 20 min at a partial pressure of 5 Torr, followed by desorption for 20 min at the same temperature. Before adsorption AN was degassed by freezing-pump-thaw cycles. For quantification of the concentrations of Lewis acid sites in titanosilicate zeolite, AN was introduced in calibrated aliquots (6 μmol g^{-1} zeolite) at room temperature to measure the ε_{2306}(LAS) molar absorption coefficient. The gradual adsorption of AN in Ti-CHA[H] zeolite resulted in a linear increase in the intensity of ν_{2306}(C≡N) band with a slope giving ε = 1.14 cm μmol^{-1}. Thus, for qualitative evaluation of the number of acid sites in Al- and Ga-CHA[H] the spectra collected after adsorption of an access of AN, followed by desorption of physically adsorbed probe molecule for 20 min were used. In contrast, a number of acid sites in Ti-CHA[H] was evaluated using the spectrum collected after adsorption of an access of AN skipping desorption step.

3. Results and discussion

Si-CHA was synthesized in a traditional fluoride media with a small amount of water [32]. Isomorphous substitution of heteroelements for Si is not only related to the structure/framework flexibility of zeolites and chemical nature of incorporated atoms but also strongly influenced by the crystallization kinetics [34]. Generally, the direct synthesis of heteroatoms-incorporated CHA[H] is considered as a challenging and slow crystallization process, especially for the synthesis of proton-form zeolites [25]. The introduced Si-CHA seeds direct the crystal growth and also accelerate the crystallization. As a result, the required time to obtain the isomorphously substituted M-CHA[H] is highly reduced with the aid of Si-CHA seeds in comparison with previously reported protocols as summarized in Table 1. For example, only 1 day is needed to obtain B-CHA[H] with high crystallinity by seeding growth, while the typical synthesis time of B-CHA[H] is 15 days [26].

Initial Si/M ratio was set to be 20 except for the B-CHA[H] because,

Table 1
Chemical compositions, synthesis time, and textural properties of M-CHA[H] (M = B, Al, Ga, and Ti) and Si-CHA.

Samples	Gel	Final products			Reference				
	Si/M	Si/M	S_{BET} ($m^2\ g^{-1}$)	V_{micro} ($cm^3\ g^{-1}$)	Time (h)	Si/M	S_{BET} ($m^2\ g^{-1}$)	Time(h)	
Si-CHA	∞	∞	647	0.30	48	∞	602	48	[32]
Al-CHA[H]	20	16.6	665	0.31	24	17.5	/	144	[35]
B-CHA[H]	5	n.d.	682	0.28	24	/	/	360	[26]
Ga-CHA[H]	20	25.7	687	0.30	72	23	/	120	[23]
Ti-CHA[H]	20	49.1	723	0.31	30	/	/	96	[48]

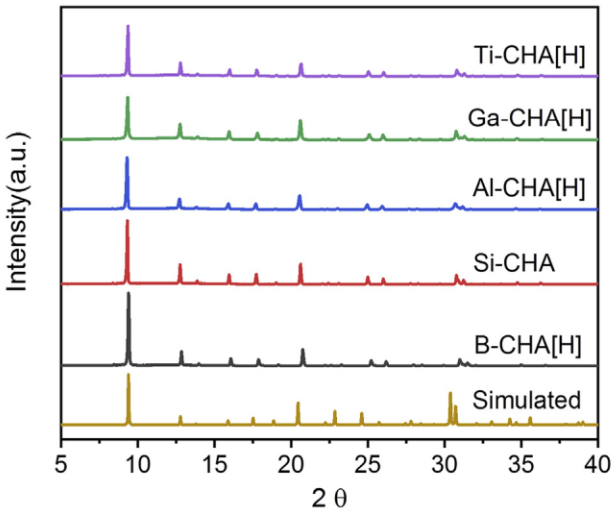

Fig. 1. Powder X-ray diffraction patterns for M-CHA[H], Si-CHA and simulated CHA.

generally, B is not easy to be incorporated into the framework of zeolites and thus high Si/B ratio was applied [2]. Chemical composition of the as-prepared M-CHA[H] was analyzed by the ICP-OES technique (Table 1). The final Si/M ratio of Al- and Ga-CHA is 16.6 and 25.7, respectively, which are in agreement with previous reports [23,35]. The Si/Ti ratio of Ti-CHA[H] is about 50, lower than Al- and Ga-CHA[H], because of the unfavorable kinetics of incorporation of Ti into zeolites [2]. The crystal structure and phase purity of all calcined products were characterized by the powder X-ray diffraction (XRD) as shown in Fig. 1. XRD patterns of all M-CHA[H] samples corresponded to that typical for **CHA** structure (Structure Commission of the International Zeolite Association). There are no diffraction lines related to other zeolite phases or heteroatoms-containing species, suggesting preservation of **CHA** structure during isomorphous substitution.

The influence of the nature of the individual heteroatoms on the size and shape of M-CHA[H] crystals was analyzed by the Scanning Electronic Microscopy (SEM), as shown in Fig. 2. The Si-CHA exhibits characteristic cubic crystals with size of ~6 μm, in agreement with previous works [30]. Introduction of B or Ti to the reaction system did not influence the shape of B-CHA[H] and Ti-CHA[H] crystals when comparing with the Si-CHA, but the crystal sizes of the B-CHA[H] and Ti-CHA[H] decreased to 4 μm and 2 μm, respectively. Noteworthy, the surface of Ti-CHA[H] crystals was smooth and no additional particles attached to the crystal surface were detected. This indicates the absence of extra-framework Ti species since the deposition of undesirable TiO_2 particles at the surface of the target crystals is typically observed for samples containing extra-framework Ti [36]. In contrast to the Si-CHA used for seeding, the Al-CHA[H] and Ga-CHA[H] tend to form small spherical particles. Interestingly, most of Al-CHA[H] crystals are composed of conjugated pairs of small and big particles. Compared to the crystal size of Si-CHA, the crystal sizes of both of Al-CHA[H] and Ga-CHA[H] decreased to 3.5 and 0.5 μm, respectively. The decreased crystal size is probably caused by the slow crystallization kinetics when the heteroelements have been incorporated [37]. For example, even though the synthesis of Ga-CHA[H] was the longest among studied chabazites (3 days), the size of Ga-CHA[H] crystal was the smallest. Decreasing crystallization time (< 3 days) results in the appearance of amorphous phase in the sample.

The isomorphously substituted M-CHA[H] zeolites were characterized using adsorption/desorption isotherms to determine the influence of the nature of heteroelements on the porosity of these materials. All the samples show similar adsorption/desorption isotherms of type I characteristic of microporous materials (Fig. 3). The textural parameters are summarized in Table 1. The BET areas and micropore volumes of all samples are in a narrow range of 647–726 $m^2\ g^{-1}$, 0.28–0.31 $cm^3\ g^{-1}$, respectively. Noticeably, all the substituted samples show higher BET area than that of Si-CHA.

To verify a successful synthesis of M-CHA[H] we firstly analyze FTIR spectra in the framework skeleton vibration region (Fig. 4A). The spectra of all M-CHA[H] zeolites under investigation show the bands attributed to stretching Si–O asymmetric (1086 and 1065 cm^{-1} for intra- and inter-tetrahedra vibrations, respectively) and symmetric (811 and 692 cm^{-1} for intra- and inter-tetrahedra vibrations, respectively) modes and the ones assigned to the 6-membered rings vibration of the D6R units (546 and 465 cm^{-1}) [38]. Systematic examination of the spectra confirmed incorporation of all metals into **CHA** framework. In particular, the shift of asymmetric vibration bands to lower frequencies for Ga-CHA[H] vs. Si-CHA evidences substitution of Si^{4+} for heavier Ga^{3+} atoms [39]. Intensive bands at 1390 and 913 cm^{-1} observed in the spectrum of B-CHA[H] are attributed to the asymmetric B–O stretching of BO_3 units in D3h symmetry and stretching vibration of B−O–Si moiety, respectively [40]. A strong fingerprint band at 960 cm^{-1} in the spectrum of Ti-CHA[H] is usually assigned to the stretching vibration of Ti−O–Si moiety in Ti-substituted zeolites [41].

The nature of OH groups covering the surface of M-CHA[H] zeolites has been studied using FTIR spectroscopy (Fig. 4B). While Si- and Ti-CHA[H] show the only band at 3743 cm^{-1} attributed to external silanol groups, Al- and Ga-substituted zeolites possess an additional band at ca. 3600–3610 cm^{-1} confirming the formation of bridging ≡Si (OH^+) M ($^-$)≡ (M = Al, Ga) groups [42]. Disappearance of absorption band ca. 3600–3610 cm^{-1} upon interaction with basic probe molecule reveals an acid character of ≡Si (OH^+) M($^-$)≡ (M = Al, Ga) groups and their accessibility for AN (Fig. 4B). Similar to the previous FTIR studies of borosilicate zeolites [40], 4 absorption bands were observed in the spectrum of B-CHA[H] in 3800–3200 cm^{-1} region (Fig. 4B). While the band ca. 3743 cm^{-1} is attributed to external silanol groups, the band ca 3705 cm^{-1} is assigned to Si–(OH)···B stretching vibration. Two other bands, observed at 3688 and 3510 cm^{-1} correspond to the vibration OH modes in B–OH and Si–OH···O groups formed upon hydrolysis of B-containing zeolites [43–45]. Thus, deep analysis of the FTIR spectra of B-CHA[H] in the region of framework (Fig. 4A) and OH-group (Fig. 4B) vibrations clearly confirms trigonal lattice oxygen environment of B^{3+} in the **CHA** framework, resulted in particular in generation of hydrogen-bonded silanol groups. Noticeably, Si–(OH)···B groups proven

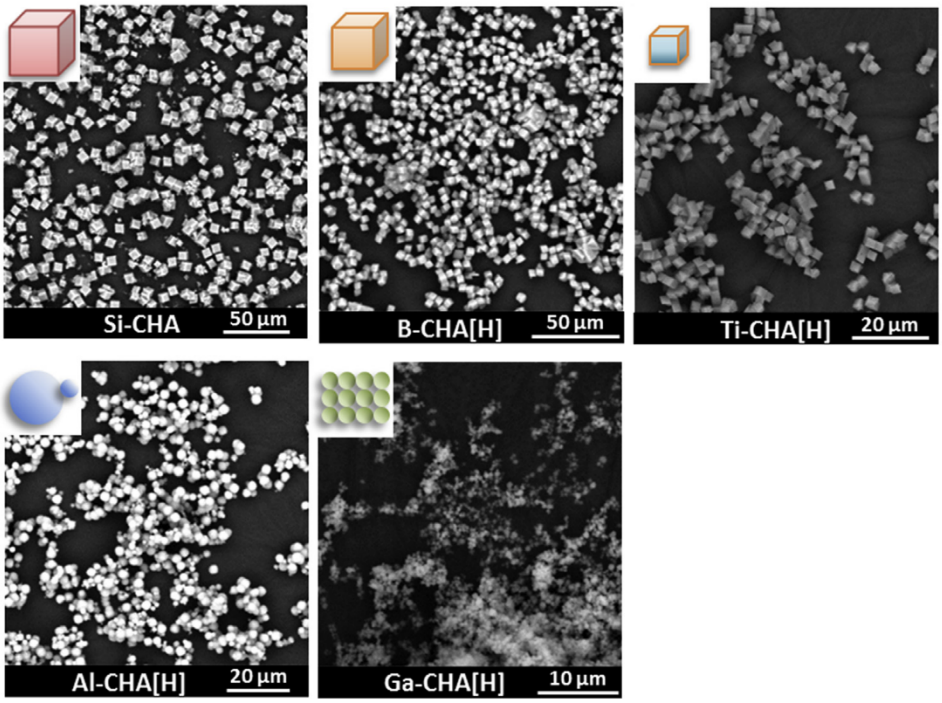

Fig. 2. SEM images of M-CHA[H] and Si-CHA.

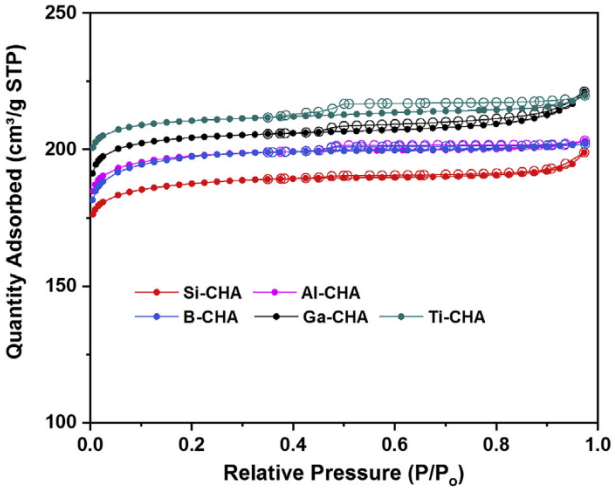

Fig. 3. Nitrogen adsorption (●) and desorption (○) isotherms of M-CHA[H] and Si-CHA.

to show acid character upon interacting with pyridine (proton affinity (PA) = 912 kJ/mol) [43], remained intact after AN (PA = 783 kJ/mol) adsorption. The result indicates weak acid strength of Si–(OH)···B groups being not sufficient for adsorbing AN at ambient temperature. In addition, the presence of B in the framework of **CHA** zeolite was also confirmed by the ^{11}B MAS NMR spectroscopy (Fig. SI-1).

The assignment of the band ca. 2304 cm^{-1} to Lewis acid sites of Ti-CHA[H] is based on the results of stepwise adsorption of small aliquots of AN monitored with FTIR spectroscopy (Fig.SI-2). In contrast to Si-CHA showing the band ca. 2275 cm^{-1} and attributed to AN interacting with Si—OH groups, the IR spectrum of Ti-CHA[H] acquired after the first doses of AN (2–30 µmol/g zeolite) showed the only characteristic peak centered at 2304 cm^{-1}, while after dosing to saturation coverages this band is convoluted with 2 other peaks corresponded to AN adsorbed at silanol groups (2275 cm^{-1}), and physisorbed AN (2265 cm^{-1}). The lower Δυ(C≡N) found for Ti-CHA[H] vs. Al- and Ga-CHA[H] reveals weaker interaction between Ti-associated Lewis acid sites and AN [46]. The weak strength of Ti-associated Lewis acid sites is also evident from substantial decreasing of 2304 cm^{-1} band with increasing outgassing time, while the intensities of respective a.b. characteristic of Al- and Ga-associated acid centres maintained with

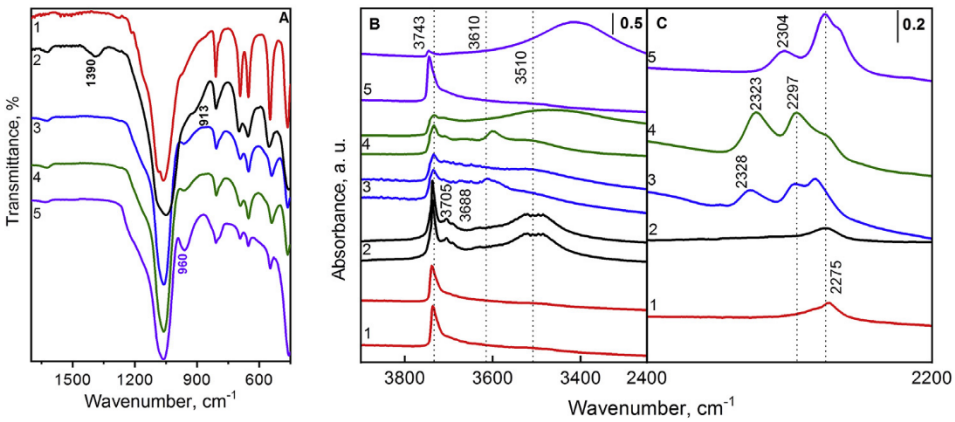

Fig. 4. FTIR spectra of M-CHA[H] zeolites: (A) region of framework vibrations; (B) region of hydroxyl vibrations before (down spectra) and after adsorption (top spectra) of d3-acetonitrile; (C) region of d3-acetonitrile vibrations (the spectrum of Ti-CHA[H] is shown after adsorption of an access of acetonitrile, while desorption of physically adsorbed probe molecule followed the adsorption step for Si-, B-, Ga-, Al-CHA[H]): Si-CHA (1), B-CHA[H] (2), Al-CHA[H] (3), Ga-CHA[H] (4), Ti-CHA[H] (5).

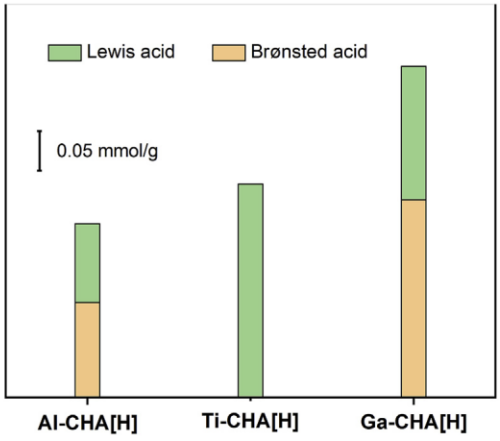

Fig. 5. Concentration of acid sites in the Al-, Ti-, and Ga-CHA[H] zeolites determined using FTIR spectroscopy of adsorbed d_3-acetonitrile.

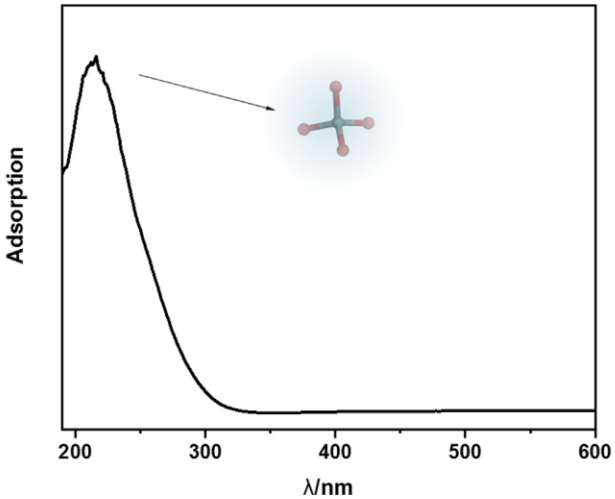

Fig. 6. UV–Vis spectrum of Ti-CHA[H], insert diagram is the tetracoordinated Ti with oxygen.

prolongation of outgassing (Fig. SI-3). Thus, in contrast to Al- and Ga-CHA, a number of acid sites in Ti-CHA was evaluated using the spectrum collected after adsorption of an access of AN skipping desorption step (Fig. 4C).

The concentration of acid sites in M-CHA[H] zeolites increased in the following sequence: Al-CHA[H] < Ti-CHA[H] < Ga-CHA[H] (Fig. 5). While Ti-CHA[H] exhibits exclusively Lewis acid sites (0.27 mmol g^{-1}), Al- and Ga-CHA[H] show sufficient amount of both Brønsted (0.12 and 0.25 mmol g^{-1}, respectively) and Lewis (0.10 and 0.17 mmol g^{-1}, respectively) acid sites. Thus, a prepared set of isomorphously substituted CHA zeolites are prospective for application as solid acid catalysts.

Many previous reports have shown that it is a challenge to introduce Ti into the framework of zeolites in a direct synthesis way because undesirable TiO_2 phases are often present in the sample [2,36]. Slow crystallization kinetics probably results in trapping of a large amount of Ti species in the extra-framework positions followed by transformation into anatase phase upon calcination [47]. As it was previously reported, it is difficult to avoid the formation of undesired TiO_2 phase by a direct synthesis to introduce Ti into the framework of CHA [48]. When the Si/Ti ratio in the final material is about 50, an obvious band at *ca.* 330 nm in the UV–Vis spectrum related to the TiO_2 is present. Even the Si/Ti has been increased, the formation TiO_2 still cannot be avoided. Therefore, to determine the type of Ti species incorporated into the Ti-CHA[H] framework, UV–Vis spectroscopy was applied. In our case, the seed-assisted synthesis protocol allows successful substitution of Ti for Si in the CHA with no undesirable TiO_2 detected. As shown in Fig. 6, the only adsorption band at *ca.* 220 nm, which is attributed to a charge transfer from oxygen to empty *d* orbitals of Ti^{4+} ions, was found in the as-prepared Ti-CHA[H]. This typical band is assigned to isolated tetrahedrally coordinated framework Ti species [49]. No extended band shoulder or peaks related to penta- or hexacoordinated extra-framework Ti species (at *ca.* 330 nm) [50,51] were observed for the Ti-CHA[H], taking account into the spectrum of Si-CHA (Fig.SI-3).

4. Conclusions

A facile way for direct synthesis of isomorphously substituted H-form M-CHA[H] (M = B, Al, Ga, and Ti) zeolites with the assistance of pure Si-CHA[H] as the crystal growth seeds has been developed in present work. The synthesis time required to obtain heteroelements substituted M-CHA[H] of high crystallinity was reduced without any decrease of the textural properties and structural ordering of substituted chabazites. The location of the incorporated heteroatoms in the framework of CHA was confirmed by the FTIR and UV–Vis spectroscopies, while no undesirable metal oxides phases were detected. This synthesis protocol has been demonstrated as a practical approach to synthesize the isomorphously substituted CHA[H] in a short time.

Acknowledgement

Authors thank Primus Research Program of the Charles University (project number PRIMUS/17/SCI/22 “Soluble zeolites”) and Neuron funding program (project number 31/2017).

Appendix A. Supplementary data

Supplementary data to this article can be found online at https://doi.org/10.1016/j.micromeso.2019.02.017.

References

[1] J. Přech, P. Pizarro, D.P. Serrano, J. Čejka, Chem. Soc. Rev. 47 (2018) 8263–8306.
[2] J. Čejka, R.E. Morris, P. Nachtigall, Zeolites in Catalysis: Properties and Applications, Royal Society of Chemistry, 2017.
[3] C.T.-W. Chu, C.D. Chang, J. Phys. Chem. 89 (1985) 1569–1571.
[4] J. Čejka, A. Vondrová, B. Wichterlová, G. Vorbeck, R. Fricke, Zeolites 14 (1994) 147–153.
[5] R. Xu, W. Pang, J. Yu, Q. Huo, J. Chen, Chemistry of Zeolites and Related Porous Materials: Synthesis and Structure, John Wiley & Sons, 2009.
[6] M.V. Shamzhy, O.V. Shvets, M.V. Opanasenko, P.S. Yaremov, L.G. Sarkisyan, P. Chlubna, A. Zukal, V.R. Marthala, M. Hartmann, J. Čejka, J. Mater. Chem. 22 (2012) 15793–15803.
[7] O.V. Shvets, M.V. Shamzhy, P.S. Yaremov, Z. Musilova, D. Prochazkova, J. Čejka, Chem. Mater. 23 (2011) 2573–2585.
[8] A. Rokicinska, M. Drozdek, B. Dudek, B. Gil, P. Michorczyk, D. Brouri, S. Dzwigaj, P. Kustrowski, Appl. Catal., B 212 (2017) 59–67.
[9] J.A. Melero, J.M. Arsuaga, P.G. de Frutos, J. Iglesias, J. Sainz, S. Blazquez, Microporous Mesoporous Mater. 86 (2005) 364–373.
[10] M.E. Davis, R.F. Lobo, Chem. Mater. 4 (1992) 756–768.
[11] K.A. Lomachenko, E. Borfecchia, C. Negri, G. Berlier, C. Lamberti, P. Beato, H. Falsig, S. Bordiga, J. Am. Chem. Soc. 138 (2016) 12025–12028.
[12] M.V. Shamzhy, C. Ochoa-Hernandez, V.I. Kasneryk, M.V. Opanasenko, M. Mazur, Catal. Today 277 (2016) 37–47.
[13] N. Koike, K. Iyoki, S.H. Keoh, W. Chaikittisilp, T. Okubo, Chem. Eur J. 24 (2018) 808–812.
[14] C. Paolucci, A.A. Parekh, I. Khurana, J.R. Di Iorio, H. Li, J.D. Albarracin Caballero, A.J. Shih, T. Anggara, W.N. Delgass, J.T. Miller, F.H. Ribeiro, R. Gounder, W.F. Schneider, J. Am. Chem. Soc. 138 (2016) 6028–6048.
[15] E. Borfecchia, P. Beato, S. Svelle, U. Olsbye, C. Lamberti, S. Bordiga, Chem. Soc. Rev. 47 (2018) 8097–8133.
[16] G. Guo, Q. Sun, N. Wang, R. Bai, J. Yu, Chem. Commun. 54 (2018) 3697–3700.
[17] J. Zhong, J. Han, Y. Wei, S. Xu, Y. He, Y. Zheng, M. Ye, X. Guo, C. Song, Z. Liu, Chem. Commun. 54 (2018) 3146–3149.
[18] B.T.W. Lo, L. Ye, G.G.Z. Chang, K. Purchase, S. Day, C.C. Tang, D. Mei, S.C.E. Tsang, Appl. Catal., B 237 (2018) 245–250.
[19] L. Han, C. Wen, Z. Wu, J. Wang, L. Chang, G. Feng, R. Zhang, D. Kong, J. Liu, Microporous Mesoporous Mater. 237 (2017) 132–139.
[20] X. Yi, K. Liu, W. Chen, J. Li, S. Xu, C. Li, Y. Xiao, H. Liu, X. Guo, S. Liu, A. Zheng, J.

Am. Chem. Soc. 140 (2018) 10764–10774.
[21] A. Damin, S. Bordiga, A. Zecchina, K. Doll, C. Lamberti, J. Chem. Phys. 118 (2003) 10183–10194.
[22] M. Moliner, C. Martinez, A. Corma, Chem. Mater. 26 (2014) 246–258.
[23] Q. Zhu, M. Hinode, T. Yokoi, J.N. Kondo, Y. Kubota, T. Tatsumi, Microporous Mesoporous Mater. 116 (2008) 253–257.
[24] Y.W. Ji, M.A. Deimund, Y. Bhawe, M.E. Davis, ACS Catal. 5 (2015) 4456–4465.
[25] C. Wen, L. Geng, L. Han, J. Wang, L. Chang, G. Feng, D. Kong, J. Liu, Phys. Chem. Chem. Phys. 17 (2015) 29586–29596.
[26] J. Liang, J. Su, Y. Wang, Z. Lin, W. Mu, H. Zheng, R. Zou, F. Liao, J. Lin, Microporous Mesoporous Mater. 194 (2014) 97–105.
[27] O. Muraza, A. Abdul-lateef, T. Tago, A.B.D. Nandiyanto, H. Konno, Y. Nakasaka, Z.H. Yamani, T. Masuda, Microporous Mesoporous Mater. 206 (2015) 136–143.
[28] G. Feng, P. Cheng, W. Yan, M. Boronat, X. Li, J.-H. Su, J. Wang, Y. Li, A. Corma, R. Xu, J. Yu, Science 351 (2016) 1188–1191.
[29] L.V. Sousa, A.O.S. Silva, B.J.B. Silva, C.M. Teixeira, A.P. Arcanjo, R. Frety, J.G.A. Pacheco, Microporous Mesoporous Mater. 254 (2017) 192–200.
[30] J. Zhang, X. Liu, M. Li, C. Liu, D. Hu, G. Zeng, Y. Zhang, Y. Sun, RSC Adv. 5 (2015) 27087–27090.
[31] K. Itabashi, Y. Kamimura, K. Iyoki, A. Shimojima, T. Okubo, J. Am. Chem. Soc. 134 (2012) 11542–11549.
[32] M.-J. Diaz-Cabanas, P.A. Barrett, M.A. Camblor, Chem. Commun. (1998) 1881–1882.
[33] B. Wichterlova, Z. Tvaruzkova, Z. Sobalik, P. Sarv, Microporous Mesoporous Mater. 24 (1998) 223–233.
[34] J. Čejka, A. Corma, S. Zones, Zeolites and Catalysis: Synthesis, Reactions and Applications, Wiley-VCH Verlag GmbH & Co. KGaA, 2010.
[35] J.R. Di Iorio, R. Gounder, Chem. Mater. 28 (2016) 2236–2247.
[36] J. Přech, Catal. Rev. 60 (2018) 71–131.
[37] N.D. Hould, R.F. Lobo, Chem. Mater. 20 (2008) 5807–5815.
[38] W. Mozgawa, M. Krol, K. Barczyk, Chemik 65 (2011) 667–674.
[39] R. Fricke, H. Kosslick, G. Lischke, M. Richter, Chem. Rev. 100 (2000) 2303–2405.
[40] R. Millini, G. Perego, G. Bellussi, Top. Catal. 9 (1999) 13–34.
[41] G. Ricchiardi, A. Damin, S. Bordiga, C. Lamberti, G. Spano, F. Rivetti, A. Zecchina, J. Am. Chem. Soc. 123 (2001) 11409–11419.
[42] S. Bordiga, C. Lamberti, F. Bonino, A. Travert, F. Thibault-Starzyk, Chem. Soc. Rev. 44 (2015) 7262–7341.
[43] J. Datka, Z. Piwowarska, J. Chem. Soc., Faraday Trans. 1 (85) (1989) 837–841.
[44] M.V. Shamzhy, O.V. Shvets, M.V. Opanasenko, L. Kuřfirtová, D. Kubička, J. Čejka, ChemCatChem 5 (2013) 1891–1898.
[45] N. Žilková, M.V. Shamzhy, O.V. Shvets, J. Čejka, Catal. Today 204 (2013) 22–29.
[46] P.E. Escalona, M.M. Peñarroya, C. Morterra, Langmuir 15 (1999) 5079–5087.
[47] P. Wu, T. Tatsumi, T. Komatsu, T. Yashima, J. Phys. Chem. B 105 (2001) 2897–2905.
[48] S. Imasaka, H. Ishii, J. Hayashi, S. Araki, H. Yamamoto, Microporous Mesoporous Mater. 273 (2019) 243–248.
[49] C. Li, G. Xiong, J. Liu, P. Ying, Q. Xin, Z. Feng, J. Phys. Chem. B 105 (2001) 2993–2997.
[50] Y. Kunitake, T. Takata, Y. Yamasaki, N. Yamanaka, N. Tsunoji, Y. Takamitsu, M. Sadakane, T. Sano, Microporous Mesoporous Mater. 215 (2015) 58–66.
[51] G. Xiong, Y. Cao, Z. Guo, Q. Jia, F. Tian, L. Liu, Phys. Chem. Chem. Phys. 18 (2016) 190–196.

nature COMMUNICATIONS

ARTICLE

https://doi.org/10.1038/s41467-019-12882-3 OPEN

Vapour-phase-transport rearrangement technique for the synthesis of new zeolites

Valeryia Kasneryk[1,5], Mariya Shamzhy[1,5], Jingtian Zhou[2,5], Qiudi Yue[1], Michal Mazur[1], Alvaro Mayoral[3], Zhenlin Luo[2*], Russell E. Morris[1,4], Jiří Čejka[1] & Maksym Opanasenko[1*]

Owing to the significant difference in the numbers of simulated and experimentally feasible zeolite structures, several alternative strategies have been developed for zeolite synthesis. Despite their rationality and originality, most of these techniques are based on trial-and-error, which makes it difficult to predict the structure of new materials. Assembly-Disassembly-Organization-Reassembly (ADOR) method overcoming this limitation was successfully applied to a limited number of structures with relatively stable crystalline layers (**UTL**, **UOV**, ***CTH**). Here, we report a straightforward, vapour-phase-transport strategy for the transformation of **IWW** zeolite with low-density silica layers connected by labile Ge-rich units into material with new topology. In situ XRD and XANES studies on the mechanism of **IWW** rearrangement reveal an unusual structural distortion-reconstruction of the framework throughout the process. Therefore, our findings provide a step forward towards engineering nanoporous materials and increasing the number of zeolites available for future applications.

[1] Department of Physical and Macromolecular Chemistry, Faculty of Science, Charles University, Hlavova 8, 128 43, Prague, Czechia. [2] National Synchrotron Radiation Laboratory, University of Science and Technology of China, 230026 Hefei, Anhui, P. R. China. [3] Center for High-resolution Electron Microscopy (CħEM), School of Physical Science and Technology ShanghaiTech University, 393 Middle Huaxia Road, 201210 Pudong, Shanghai, China. [4] EaStCHEM School of Chemistry, University of St Andrews, Purdie Building, St Andrews KY16 9ST, UK. [5] These authors contributed equally: Valeryia Kasneryk, Mariya Shamzhy, Jingtian Zhou. *email: zlluo@ustc.edu.cn; maksym.opanasenko@natur.cuni.cz

Zeolites are crystalline porous materials used for many applications, including gas separation and catalysis[1–3]. Although millions of thermodynamically stable structures have been predicted under ambient conditions, until now, the zeolite community has only recognised ~250 different zeolite topologies[4]. Such discrepancy between the numbers of proposed zeolite topologies and those produced via traditional hydrothermal approaches has prompted the development of alternative strategies for zeolite synthesis. These new strategies include both direct (e.g., using phosphorus-containing cations[5,6], metal complexes[7] or proton sponges[8] as structure-directing agents) and post-synthesis (3D-3D transformation at high pressures >1 GPa[9]; 3D-2D-3D transformation known as ADOR[10]) methods. However, most of these approaches use a trial-and-error tactic, except for ADOR[11]. ADOR is a unique approach because the topology of new zeolites can be easily predicted based on the knowledge of the parent structure. ADOR strategy was successfully applied for the structural reconstruction of several germanosilicate zeolites such as **UTL**[10], **UOV**[12] and ***CTH**[13] (three-letters codes are assigned to established structures of zeolites that satisfy the rules of the IZA Structure Commission). However, attempts to transform other potential structures (e.g., **IWW**, **ITH** and **ITR**, among others) using this approach have been unsuccessful thus far because "open framework" zeolite layers containing pores perpendicular to the layer plane are highly labile, resulting in the complete degradation of the zeolite layers or, at best, in the reconstruction of the initial zeolite framework with a chemical composition different from that of the parent material[14].

Here, we report a straightforward strategy to construct new zeolites through non-contact vapour-phase-transport (VPT) rearrangement at room temperature. This method offers the opportunity to prepare new zeolite topologies otherwise inaccessible by both hydrothermal and conventional ADOR synthesis routes. We have used a combination of in situ (XRD, XANES) and ex situ (NMR) techniques to follow the rearrangement process and to study the mechanism of VPT transformation involving intermediate structures. Diffraction, adsorption and microscopy data unambiguously showed that the transformation of **IWW** germanosilicate into the new zeolite phase (designated as IPC-18) proceeds without degradation of zeolite layers and thus affects only interlayer structure units without defects from structural rearrangement.

Results

3D-2D-3D zeolite transformation. The unsuccessful application of the ADOR strategy for the 3D-2D-3D transformation of specific zeolites, including **IWW**[14], prompted us to develop alternative approaches for controllable disassembly-reassembly of appropriate zeolite frameworks containing labile structural units. The key step in such transformations is the hydrolysis of labile bonds (typically, Si–O–Ge or Ge–O–Ge) in double-four-ring (D4R) units connecting zeolite layers[15]. Severe hydrolysis conditions and inappropriate chemical composition of parent materials are among the most common reasons for the partial deterioration or even full collapse of zeolite frameworks during the disassembly[16]. Three types of germanosilicates with general formula $Si_xGe_{1-x}O_2$ and with chemical compositions ($Si/Ge = x/(1-x)$) similar to those used for conventional ADOR transformations[16] were chosen to implement the VPT 3D-2D-3D rearrangement: **UTL** (Si/Ge = 4.2), **UOV** (Si/Ge = 3.1) and **IWW** (Si/Ge = 3.7). The structures of these initial germanosilicates are schematically shown in Fig. 1 as the combinations of dense (for **UTL**) or porous (**UOV**, **IWW**) layers and double-four-ring (D4R) building units connecting the layers. Because **UTL** and **UOV** zeolites have been already transformed into respective daughter zeolites by conventional ADOR strategy[12,17], they were chosen in this study as reference materials to evaluate any differences between VPT and conventional ADOR approaches for known {parent zeolite–daughter zeolite} pairs. For the VPT transformation of the selected zeolites, a thin layer of zeolite powder was placed in the reactor containing a membrane permeable to vapours of low-molecular mass reactants located at the bottom part of the reactor (Fig. 1). The rearrangement of the zeolite was initiated by the interaction between acid vapour (12 M water solution of HCl with $p_{H2O} = 10$ mm Hg and $p_{HCl} = 23$ mm Hg at 303 K[18]) and the frameworks{–Si–O–Ge–} + HCl → {–Si–OH} + {Cl–Ge–}.

Volatile germanium chloride ($bp_{GeCl4} = 359$ K, for pure $GeCl_4$ $p_{GeCl4} = 94$ mm Hg at 300 K[19]) resulting from this interaction is adsorbed/dissolved and hydrolysed in the water solution ($GeCl_4 + nH_2O \rightarrow Ge(OH)_nCl_{4-n} + nHCl$), at the bottom of reactor. Such an approach allows unrestricted mass transport of the species formed by destruction of the most labile Ge-rich connecting units but avoids the deep reconstruction of the germanosilicate framework mediated by water.

Condensation of silanols ({–Si–OH} + {–Si–OH} → {Si–O–Si} + H_2O), formed during the hydrolysis, resulted in the formation of the respective daughter structures from parent zeolites (Fig. 1). The extent of the structural rearrangement differs among the zeolites used. Treatment of **UTL** leads to the formation of the known IPC-7 material (Supplementary Fig. 1) with alternating connectivity between layers through single-four-ring (S4R) and D4R units[17], whereas transformation of **UOV** results in the formation of the recently reported IPC-12 zeolite (Supplementary Fig. 1) with direct connectivity between layers, instead of the D4R units that are present in the initial framework[12]. The transformation of **IWW** results in the formation of a structure in which the layers are exclusively connected through S4R units (see discussion of this structure below). Therefore, the building units formed through VPT rearrangement depend on the structure of initial zeolite: the presence of pores in the layers of **UOV** and **IWW** zeolites results in facilitated mass transport and thus in the formation of S4R (for **IWW**) or O-bridge (for **UOV**) units, whereas treatment of **UTL** with non-porous layers produces material with alternating D4R/S4R units, under the same conditions.

IPC-7 (derivative of **UTL**) and IPC-12 (derivative of **UOV**) materials obtained using liquid-phase ADOR method don't have any major difference in properties with their analogues synthesised by VPT. In contrast, the open framework of layers in **IWW** zeolite cannot withstand the conventional ADOR treatment. Nevertheless, at room temperature, VPT yields an intermediate derivative (denoted as IPC-18P, Supplementary Fig. 2) that can be condensed at high temperatures to form the highly crystalline IPC-18 zeolite. The formation of S4R, but not D4R + S4R or O-bridge connections, between layers of IPC-18 can be explained as follows. A simulation study[20] predicted the **IWW** derivative with S4R connections to have lower formation enthalpy (by 3.5 kJ mol^{-1}) than the structure with O-bridges. Conversely, under the conditions applied, mass transport can be inhibited during the transformation. Low-molecular weight siliceous products of hydrolysis of D4R units can remain in the zeolite pores and subsequently participate in condensation to form S4R units, as observed in some ADORable zeolites, such as **OKO**[21]. As expected, the final IPC-18 material is significantly Ge-depleted (Si/Ge decreased from 3.7 to 65.0), thus indicating that germanium atoms are successfully removed from the **IWW** framework through the formation of volatile species (presumably $GeCl_4$).

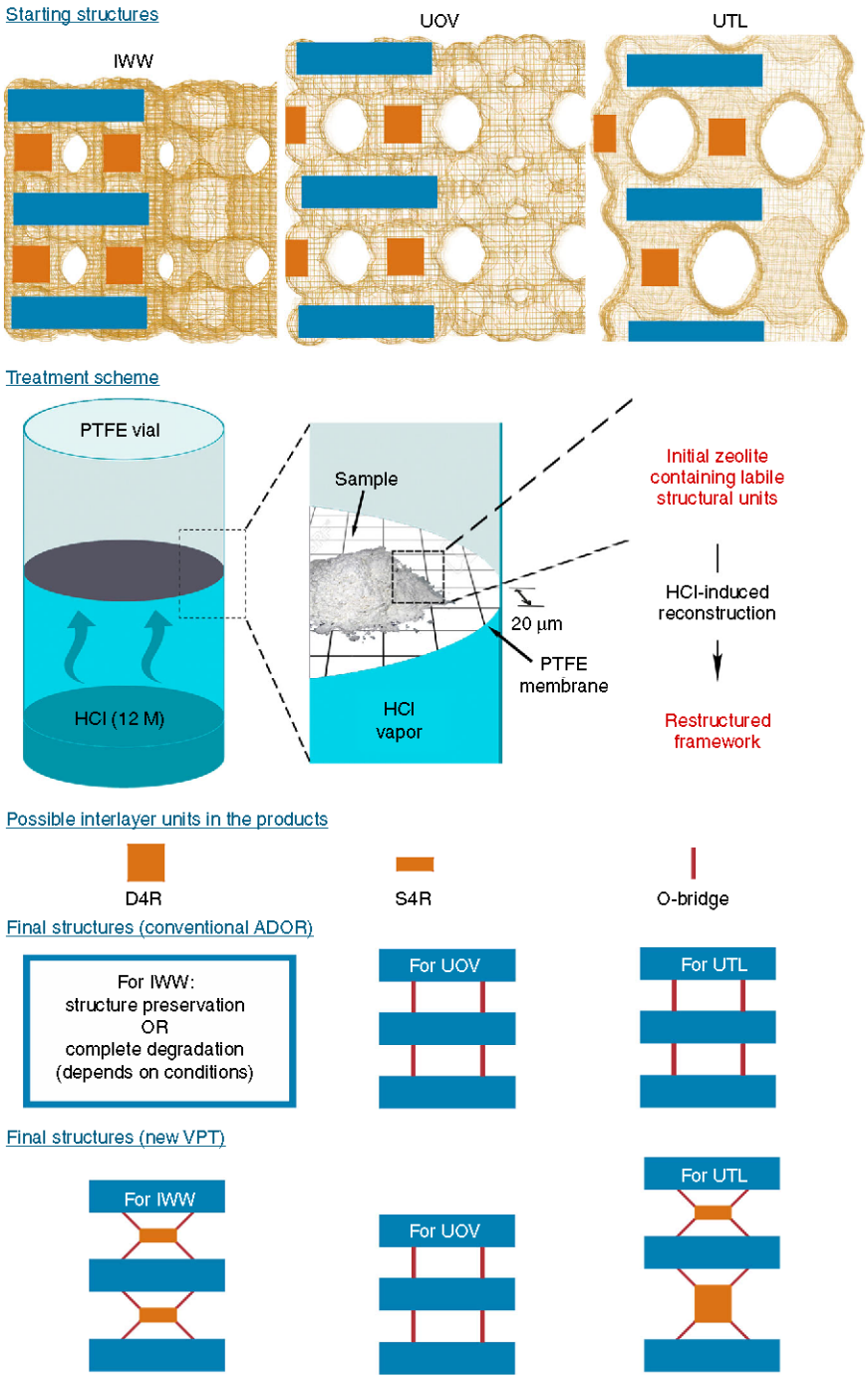

Fig. 1 Starting materials for VPT and respective products. Structures of initial zeolites are porous frameworks composed of layers (blue tetragons) and connecting D4R units (orange squares). Vapour of HCl (blue on treatment scheme of the VPT method) interacts with solid zeolite resulting in structural transformation accompanied by leaching of Ge atoms probably as $GeCl_4$. Respective D4R units can be either reconstructed to S4Rs or decomposed. Final structures obtained via conventional ADOR and VPT rearrangement of the parent zeolites (**IWW**, **UOV** and **UTL**) are different due to the difference in layers porosity, thus in the interlayer species diffusion rate

Structural features of IPC-18 vs parent IWW. The XRD pattern of IPC-18 matches well that of the theoretically predicted framework (Fig. 2a). Based on Rietveld refinement of the final structure (Fig. 2b, c), the space group was identified as $P2_1/c$, which differed from the parent **IWW** (*Pbam*). The following parameters of the cell were determined: $a = 9.606(4)$ Å, $b = 12.7280(21)$ Å, $c = 40.717(7)$ Å, $\alpha = 90.0°$, $\beta = 94.97°$, $\gamma = 90.0°$. The parent **IWW** zeolite has a 3D pore system with 8- and 12-ring channels, which are both intersected by sinusoidal 10-ring channels. After VPT rearrangement, 8- and 12-ring pores located along the 001 projection remain intact, whereas 10-ring pores become eight-ring pores due to the transformation of D4Rs into S4Rs. This transformation of the pore system resulted in decreased micropore volume and average pore size (Fig. 2d, e). The micropore volume of IPC-18 is 1.7 times lower than that of the initial **IWW** sample (0.172 vs. 0.104 $cm^3 g^{-1}$, respectively). The average channel diameter decreases from 0.63 nm, for **IWW**, to 0.58 nm, for IPC-18. Despite differing in micropore volume and size, both parent and daughter zeolites show the same {mesopore + interparticle} volume (0.025 $cm^3 g^{-1}$) and similar

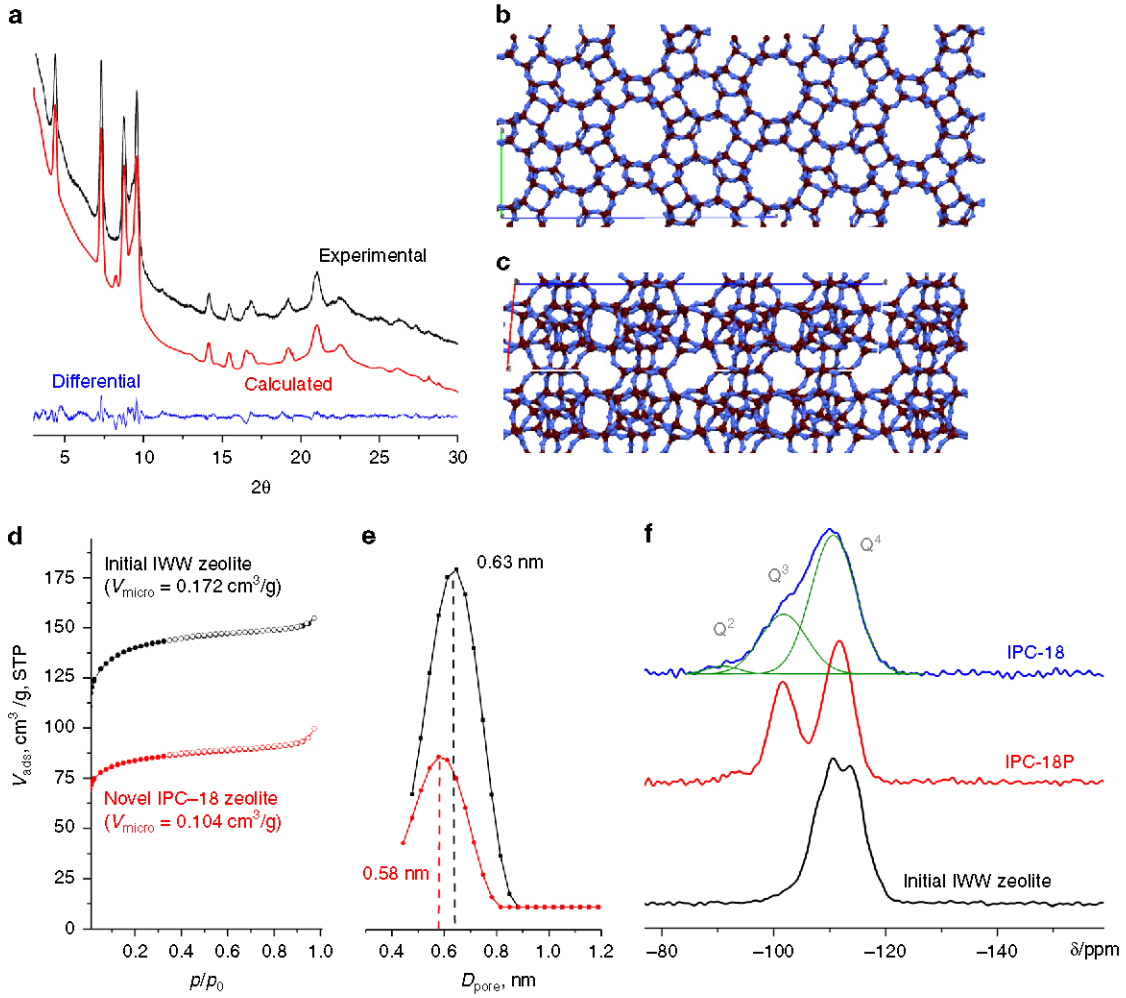

Fig. 2 Basic characterisation of IPC-18. **a** XRD patterns of IPC-18: experimental (black), calculated after Rietveld refinement (red), and the difference between them (blue); **b**, **c** crystallographic models of IPC-18 in the *ab* projection demonstrating 12 and 8-ring pores (**b**), and in *ac* projection, showing connectivity between layers through S4R units (**c**); **d** nitrogen adsorption and desorption isotherms for parent **IWW** and daughter IPC-18 zeolites; **e** pore size distribution for initial **IWW** (black) and final IPC-18 (red); **f** ^{29}Si MAS NMR spectra of **IWW**, intermediate IPC-18P and IPC-18 samples

morphology of the crystals, ~1 μm in size (Supplementary Fig. 3). This result indicates that no significant fraction of additional pores, which would influence the textural properties of IPC-18, is created during the VPT transformation. This is an important conclusion because the state of framework silicon atoms is significantly changed in the course of the structural transformation.

Solid-state ^{29}Si MAS NMR analysis of **IWW**, intermediate IPC-18P and IPC-18 shows the evolution of the degree of condensation of silanols in this process (Fig. 2f). The spectrum of the starting **IWW** is characterised by the presence of a signal at −115 ppm, which corresponds to Q^4 Si atoms. VPT treatment results in the hydrolysis of most of Si–O–Ge bonds and formation of the IPC-18P precursor, which increases the intensity of silanol groups (Q^3 atoms, −101 ppm) in the spectrum. The spectrum of IPC-18P also contains a low-intensity peak at −93 ppm, which can be related to Q^2 silicon atoms. This is an unusual feature of the zeolitic intermediate obtained by disassembly because a recent in situ NMR study revealed only Q^3 Si among deficient atoms during a top-down structural transformation of germanosilicate[15]. Subsequent thermal treatment of IPC-18P decreases the intensity of the signal attributed to silanol groups due to topotactic condensation of the zeolite layers into a 3D structure, with no evidence of additional defects in IPC-18 due to the reconstruction of the pore system in **IWW**. However, the NMR spectrum of the final IPC-18 still contains quite intense (25–30 % of overall area fraction) Q^3 signal (Fig. 2f). IPC-18 synthesis (IPC-18P reassembly) temperature lower than optimal can be the reason for relatively high content of silanols in final material. In addition, some Ge atoms are still remained in IPC-18 framework as Si(OGe)(OSi)$_3$ domains that give a peak, which can overlap with the Q^3 peak.

Structural differences and similarities between the parent **IWW** and its derivative can be directly observed through spherical aberration corrected (C_s-corrected) Scanning Transmission Electron Microscopy (STEM) analysis of the respective materials (Fig. 3). Images collected from the top view of the layers (Fig. 3a, c) along the [100] orientation show the same member rings and the same pore arrangements, thus confirming their preservation during the VPT treatment, as well as topotactic condensation. Along this orientation, the D4Rs that are affected by the hydrolytic process are not visible in these top views. Therefore, after collecting data from the side view along [010], the interlayer distances significantly decreased due to changes in D4Rs which have now turned into S4Rs. The projected measured distance between "T" atoms for a D4R is ~3.1 Å. Thus, initially, a decrease of ~3 Å should be expected. The distances between layers directly measured on high-resolution images are 12.23 Å for **IWW** and 9.11 Å for IPC-18, in very good agreement with the

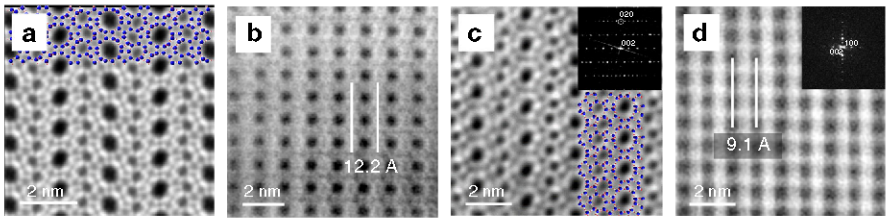

Fig. 3 Comparison of different projections of IWW and IPC-18. C_s-corrected STEM-ADF images of **IWW** (**a**, **b**) and IPC-18 (**c**, **d**) zeolites: **a**, **c**—top [100] view of the layers, which remain intact during the VPT rearrangement (crystallographic models of the same layer are superimposed for clarity), **b**, **d**—side [010] view showing the decrease in interlayer distance caused by the transformation of D4Rs into S4Rs

transformation of the linking units. Selected area electron diffraction (SAED) and/or Fourier diffractograms (FD) measurements were also collected along different orientations (see Fig. 3 insets), which clearly showed, first, the good crystallinity of the materials, with no additional structural defects, and, second, the formation of S4Rs. The analysis of HRTEM images collected in three projections of **IWW** crystals (Supplementary Fig. 4a–c) and IPC-18 (Supplementary Fig. 4d–f) confirms the aforementioned conclusion about the direction in which the anisotropic structural transformation occurs. For one projection [001], d-spacing is the same (12.0 Å) for both parent and daughter zeolites. The major difference between **IWW** and IPC-18 is the connectivity between layers (Supplementary Fig. 4).

Mechanism of VPT zeolite rearrangement. Characterisation of the starting and final zeolite structures is relatively simple because they are crystalline materials with well-ordered frameworks. In contrast to the relatively stable IPC-18P layered material, any intermediate structures formed during the **IWW**-to-IPC-18P transformation (hydrolysis) or during the IPC-18P-to-IPC-18 condensation (reassembly) are hardly detectable without in situ methods as both processes are completed within 1 h. We used in situ XRD to trace the diffraction peaks with different Miller indices *hkl*-related to different directions in the structures of the treated materials (*hkl* ($l \neq 0$) interlayer peaks, with varying positions over time, and intralayer *hk0* reflections, which should maintain the positions) to shed the light on the whole mechanism of **IWW**-to-IPC-18 transformations (a general scheme is presented in Fig. 4e). In addition, we performed quantitative lattice analysis based on XRD patterns and followed the local state of the Ge atoms by in situ XANES during the VPT rearrangement to identify the relationship between the nature of leaving atoms and framework features at each stage of the structural transformation.

Immediately after starting the treatment (<1 min), the positions of *00l* reflections shifted to higher angles (Fig. 4a), indicating a decrease in d-spacing caused by disassembly of D4R connecting units. Surprisingly, the positions and intensities of *hk0* reflections (110 and 400 are the most representative, Fig. 4a) are also significantly changed already at the first step of hydrolysis (0–2 min under conditions used). Analysis of the correlation between unit cell parameters and treatment time provided further insight into the processes that occur during the first step of the VPT (Fig. 4c). Not only the interlayer *c* parameter but all lattice constants (*a*, *b*, *c*) considerably change during this step, indicating partial distortion of the structure of **IWW** layers (illustrated on Fig. 4e). Simultaneously, the β angle, which is indicative of the shift of layers relative to each other, remains unchanged in the first step. Thus, at this stage, the layers become flexible but are still stacked, most likely due to ionic interactions and hydrogen bonding between interlayer species—primary products of hydrolysis. In situ XANES (Fig. 4d) revealed the major change in the nature of Ge atoms during this period since the Ge K-edge (E_0) steeply and linearly decreased over time at the same stage (0–2 min) because most Ge–OT^{IV} (T^{IV} = Si or Ge) bonds predominantly located at D4R units were broken. The intensity of some XRD reflections (related to both inter- and intralayer planes, e.g., 110 and 111) decrease in the first step of the VPT transformation, suggesting a complete loss of structural ordering in the respective directions of the lattice.

During the second step of hydrolysis (from 2 to 10–12 min), the aforementioned reflections appear at slightly shifted positions, indicating at least a partial recovery of the respective framework ordering. At first sight, the positions of the other *hkl* ($l \neq 0$) reflections continue the gradual right-shift in the second stage of the rearrangement (Fig. 4a). However, the behaviour of the respective lattice constant (*c*) is more complex (Fig. 4c): after a series of minor changes (at ~½, 2, 3 min when *c* parameter is either slightly decreased or increased), *c* starts to decrease, with a clear exponential decay trend (Fig. 4c, blue line) until the end of the procedure. The parameters *a* and *b* monotonically decrease during the second step of hydrolysis, whereas β peaks around 90.7°, indicating a slight, transient shift of the layers relative to each other during the structural reorganisation of the layers. These processes are accompanied by a linear change in E_0 as a function of time in XANES spectra, which is slower than the first step (Fig. 4d). Additional peaks around $E = 11120$ and 11125 eV appear in XANES spectra at this stage (Supplementary Fig. 7), indicating an accumulation of hydrolysed Ge species extracted from the framework. Overall transformations during this period can be attributed to a slow hydrolysis of isolated Ge–O bonds remaining after primary decomposition of the D4Rs (major fraction) and extraction of Ge atoms located in zeolite layers (minor fraction because the layers are almost purely siliceous). Completion of the D4R disassembly and removal of intercalated species allows the partial recovery of layer organization as the parameters *b* and β return to the original values after 12 mins of treatment.

At the final, third, step of the VPT rearrangement (12 + min), most XRD reflections maintain their positions and intensities, and only a few *hkl* ($l \neq 0$) reflections, such as 001 and 313, show changes in their intensity after 12 min (Fig. 4a), similarly to the lattice parameters (Fig. 4c) and to the Ge state, which remains virtually unchanged during the final stage of hydrolysis (Fig. 4d).

Heating the intermediate IPC-18P material up to ~500 K has no effect on the positions or intensities of intralayer *hk0* reflections, highlighting a complete layer rearrangement during the hydrolysis step of the VPT transformation (Fig. 4b). In contrast, the position of the 001 reflection in relation to the interlayer distance gradually shifts in the range of $T = \mathrm{RT} - 350$ K, being almost constant at temperatures of 350–450 K. Further increasing the temperature results in a gradual collapse of the IPC-18 zeolite framework, accompanied by a shift in all XRD reflections at $T = 450$–650 K and in a decrease of their intensities at T >650 K (Fig. 4b). Based on our in situ XRD and XANES data, we propose the following mechanism of **IWW**-to-IPC-18 transformation, as illustrated in Fig. 4e:

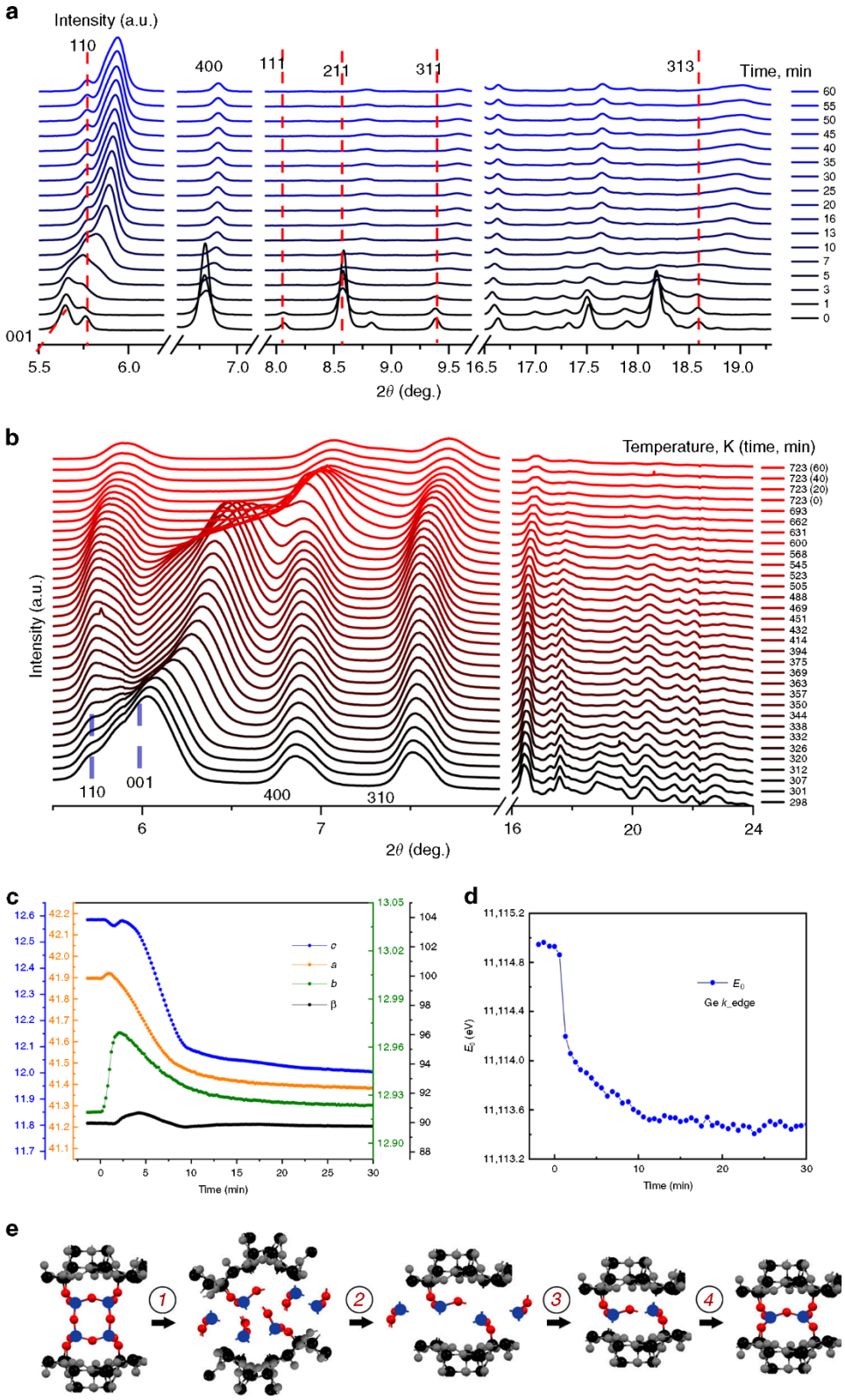

(1) fast hydrolysis of Ge-rich linking units and partial distortion of the silicon-enriched layers at RT (0–2 min under the conditions used in this study);

(2) intermediate extraction of the remaining Ge atoms accompanied by partial reconstruction of the initial framework, particularly of the layers (2–12 min);

(3) slow rearrangement of the species remaining in the interlayer space until reaching the equilibrium state at RT (>10–12 min)

(4) layers condensation (reassembly) at slightly increased temperatures (up to 350 K) with no effect on the structure of the layers.

Fig. 4 In situ data supporting the assumed mechanism of VPT. **a** In situ XRD demonstrating changes during the hydrolysis of the parent **IWW** zeolite; **b** in situ XRD collected during thermal treatment of IPC-18P; **c** variation of lattice parameters (lengths in Å and angle in degree) as a function of time during the VPT treatment; **d** evolution of the primary line extracted from in situ XANES spectra representing changes in Ge state during hydrolysis steps; **e** proposed mechanism (Si and Ge atoms are not distinguished for clarity and only structural, but not chemical, changes are shown). Full in situ XRD data, lattice parameters and XANES profiles are shown in Supplementary Figs. 5, 6 and 7, respectively. Analysis of the variation of lattice parameters and position of primary line in XANES spectra allows to distinguish several steps during VPT. Unexpectedly, the disassembly of Ge-rich D4Rs was accompanied by partial disorder of the layers, which become more crystalline on the second step of hydrolysis. The topology of resulting layers only slightly differs from that of starting zeolite. Following deintercalation of interlayer debris and condensation allows the formation of new IPC-18 zeolite

The VPT rearrangement technique was developed and first exemplified for the ADOR transformation of different germanosilicate zeolites characterised by the unidirectional location of Ge-enriched D4R units (i.e., **UTL**, **UOV**, **IWW**). The VPT approach overcomes the limitations of the classical ADOR approach for the rational design of zeolites. Although VPT treatment of **UTL** and **UOV** germanosilicates produces known ADORable IPC-7 and IPC-12 zeolites of high crystallinity, VPT rearrangement of the **IWW** framework enabled preparation and structure refinement of the previously predicted, yet thus far inaccessible, IPC-18 zeolite via existing synthesis approaches. In situ XRD and XANES studies on the VPT rearrangement of **IWW** revealed the acid-induced reorganisation of not only interlayer but also intralayer framework domains, resulting in the temporary disordering of the structure followed by its reconstruction to a well-ordered material with a different framework from the parent zeolite. The successful application of VPT rearrangement to germanosilicate zeolites of different topologies highlights the potential of this technique for the 3D-3D transformation of crystalline materials with labile frameworks collapsing upon contact with the solvent (e.g., ordered organic-free germanates or some metal-organic frameworks). In combination with other methods for post-synthesis alteration of 3D frameworks, this approach makes it possible to manipulate the structures of anisotropically labile materials.

Methods

Synthesis of MPPH. The structure-directing agent (SDA) for IWW synthesis is 1,5-Bis-(methylpyrrolidinium)pentane dihydroxyde (MPPH), which was prepared according to[22]. In total, 40 g of *N*-methylpyrrolidine (Sigma Aldrich, 97%) was mixed with 37.5 g of 1,5-dibromopentane (Sigma Aldrich, 97%) in 300 ml of acetone (Lachner, 99.99%) and heated under reflux for 24 h. The resulting 1,5-bis-(methylpyrrolidinium)pentane dibromide was then ion-exchanged into th ehydroxide form using Ambersep® 900(OH) an anion exchange resin (Acros Organics, 0.8 mmol of SDA per 1 g of anion exchange resin). The solution was concentrated under low pressure (35 Torr) at 303 K until the hydroxide concentration was ~1.0 M.

Synthesis of DMAH. (6R,10S)-6,10-dimethyl-5-azoniaspiro[4,5] decane hydroxide (DMAH), the SDA for the synthesis of germanosilicate **UTL**, was prepared based on the procedure reported in Ref. [23]. In total, 16.07 g of (2R,6S)-2,6-dimethylpiperidine (Sigma Aldrich, 98%) was added drop-wise to 140 ml of water solution containing 5.68 g of sodium hydroxide (Penta, 98%) and 30.66 g of 1,4-dibromobutane (Aldrich, 99%). Subsequently, the mixture was refluxed under intensive stirring for 12 h. After cooling in an ice bath, an ice-cooled 50% (wt.) solution of NaOH (70 ml) was added, and further solid NaOH was added until forming the oil product. After crystallisation, the solid was filtered and extracted with chloroform (Lachner, 99.92%). The organic fraction was dried, using anhydrous sodium sulphate (Sigma Aldrich, 99%), and partly evaporated (50–100 mL of residual volume); then, diethyl ether (Lachner, 99.97%) was added to the remaining mixture. The final solid product was washed three times with diethyl ether. The bromide salt was ion-exchanged into the hydroxide form using an Ambersep® 900 (OH) anion exchange resin (0.8 mmol of SDA per 1 g of anion exchange resin) and concentrated by evaporation to prepare a 1 M solution.

Synthesis of IWW zeolite. IWW zeolite samples was performed according to Ref. [22] from the reaction mixture 0.66 SiO_2: 0.33 GeO_2: 0.25 MPPH: 15 H_2O. Appropriate amounts of germanium dioxide (Sigma Aldrich, 99.99%) and tetraethyl orthosilicate (Sigma Aldrich, 98%) were added to the SDA solution under stirring. The resulting mixtures were stirred to evaporate the ethanol formed by hydrolysis of tetraethyl orthosilicate. Then, the gels were heated in Teflon-lined stainless steel autoclaves at 448 K for 11 days. The final products were recovered by centrifugation, washed with water and dried at 333 K overnight. The resulting solids were calcined at 853 K for 6 h in air.

Synthesis of UTL zeolite. UTL zeolite samples was based on the method reported in Ref. [23] by crystallisation of a gel with the composition of 0.66 SiO_2: 0.33 GeO_2: 0.25 DMAD: 30 H_2O, at 448 K for 6 days under agitation (60 rpm). The solid products were separated by filtration, washed out with distilled water, and dried overnight at 368 K. The final solids were calcined at 823 K for 6 h with a temperature ramp of 2 K min^{-1} under air flow (200 ml min^{-1}).

Synthesis of UOV zeolite. Samples of germanosilicate UOV were prepared according to Ref. [24] from reaction mixtures with the following composition: 0.33 SiO_2: 0.66 GeO_2: 0.25 DMDH: 10 H_2O, using decamethonium dihydroxide (DMDH) as the SDA. DMDH was previously prepared from the bromide form by ion exchange using Ambersep® 900(OH) anion exchange resin. The solution of DMDH was concentrated under low pressure (25 Torr) at 303 K until an SDA concentration >1.5 M. Some germanium oxide was dissolved in a mixture of water and DMDH. Silica (Cab-O-Sil M5, Supelco Analytical) was gradually added to the solution, and the mixture was stirred at room temperature for 30 min. The reaction gels were autoclaved at 448 K for 7 days under static conditions. The solid product was recovered by centrifugation, washed several times in distilled water until the pH of the solution became neutral, dried at 338 K during 12 h, and finally calcined at 823 K for 6 h with a temperature ramp of 2 K min^{-1} under air flow (200 ml min^{-1}).

VPT treatment. In total, 0.1 g of calcined zeolite was placed in the reactor containing polytetrafluoroethylene (PTFE) membrane over 10 ml of 12 M hydrochloric acid solution (p. a., Penta) at 298 K for $\tau = 5$ min–48 h. Caution: the VPT procedure uses concentrated HCl. Standard laboratory practice for dealing with highly corrosive liquids (including appropriate personal protective equipment) should be used.

Basic characterisation. The structure and crystallinity of zeolites were determined by powder X-ray diffraction using a Bruker AXS D8 Advance diffractometer with Cu Kα radiation in Bragg-Brentano geometry. The chemical composition was determined on an ICP/OES (ThermoScientific iCAP 7000). Adsorption experiments were performed using nitrogen as a probe molecule. Ad-/desorption isotherms were measured using an ASAP 2020 (Micrometeritics) static volumetric apparatus at liquid nitrogen temperature (−196 °C). Before the sorption measurements, all samples were degassed with a turbomolecular pump at 523 K for 4 h. The micropore volume was estimated by application of the t-plot method, and the pore size distribution was obtained using the NLDFT method. The morphology of the samples was determined under a scanning electron microscope (SEM) TESCAN Vega. Solid-state ^{29}Si *NMR* spectra were recorded on an Agilent DD2 500WB spectrometer at a resonance frequency of 99.30 MHz. MAS NMR measurements were carried performed with a commercial 3.2 mm triple resonance MAS probe. The chemical shifts of ^{29}Si are referenced to tetramethylsilane at 0 ppm.

Synchrotron XRD. The in situ synchrotron XRD was performed at the BL14B and BL19U2 stations of the Shanghai Synchrotron Radiation Facility (SSRF). The wavelength of incident X-ray photons was 0.1240 nm, and the diffraction patterns were recorded using two-dimensional X-ray detectors. To monitor the hydrolysis process in real-time, the sample was sealed in a homemade cell with Kapton windows. Diffraction patterns from the sample were continuously recorded with an exposure time of 10 s per frame and with an interval of 2 s between adjacent frames. The beginning of reaction was controlled by an electric pump, which injected concentrated hydrochloric acid into the cell to initiate the hydrolysis. For the in situ heating experiment, the sample was placed on a heating stage. The temperature was increased from room temperature to 723 K at a rate of 1.5 K per minute and was then kept at 723 K for 1 h. Diffraction patterns were continuously recorded at an exposure time of 100 s per frame and at an interval of 20 s between adjacent frames.

Quantitatively analysis for the lattice parameters. For the XRD patterns obtained during the in situ hydrolysis step of the VPT transformation, the time-dependent peak positions of reflections (001), (320), (400), (120), (311), (310)

and (211), as shown in Fig. SI-6, are used to calculate the quantitative lattice information with the fsolve function in Matlab, assuming a monoclinic crystalline structure for the materials.

Synchrotron XANES. Ge K edge XANES measurements were performed at the beamline 1W1B of the Beijing Synchrotron Radiation Facility (BSRF). The spectra were collected in the transmission Q-XAFS mode to monitor the hydrolysis reaction, with a rate of 37.6 s per spectrum. During the experiment, the sample was sealed in the homemade cell, as described above.

Electron microscopy. Electron microscopy analyses were performed in a coldFEG JEOL Grand ARM 300 electron microscope. The microscope was equipped with a double corrector from JEOL assuring a spatial resolution of 0.7 Å when operated at 300 kV. Before observation, the samples were deeply crushed using a mortar and pestle and dispersed in ethanol. A few drops of the suspension were deposited on a holey carbon copper microgrids. For imaging, both Annular Dark Field and Annular Bright Field detectors were used simultaneously, acquiring data in both detectors.

Data availability

XRD, NMR, adsorption and in situ XRD data were deposited at 10.6084/m9.figshare.9853502 and 10.6084/m9.figshare.9853505. All the data that support the findings of this study are available from the corresponding authors upon reasonable request

Received: 11 July 2019; Accepted: 26 September 2019;
Published online: 12 November 2019

References

1. Weckhuysen, B. M. & Yu, J. Recent advances in zeolite chemistry and catalysis. *Chem. Soc. Rev.* **44**, 7022–7024 (2015).
2. Přech, J., Pizarro, P., Serrano, D. P. & Čejka, J. From 3D to 2D zeolite catalytic materials. *Chem. Soc. Rev.* **47**, 8263–8306 (2018).
3. Shamzhy, M., Opanasenko, M., Concepción, P. & Martínez, A. New trends in tailoring active sites in zeolite-based catalysts. *Chem. Soc. Rev.* **48**, 1095–1149 (2019).
4. Kuznetsova, E. D., Blatova, O. A. & Blatov, V. A. Predicting new zeolites: a combination of thermodynamic and kinetic factors. *Chem. Mater.* **30**, 2829–2837 (2018).
5. Corma, A. et al. Extra-large pore zeolite (ITQ-40) with the lowest framework density containing double four- and double three-rings. *Proc. Natl Acad. Sci. USA* **107**, 13997–14002 (2010).
6. Simancas, R. et al. A new microporous zeolitic silicoborate (ITQ-52) with interconnected small and medium pores. *J. Am. Chem. Soc.* **136**, 3342–3345 (2014).
7. Xu, Y., Li, Y., Han, Y., Song, X. & Yu, J. A Gallogermanate zeolite with eleven-membered-ring channels. *Angew. Chem., Int Ed.* **52**, 5501–5503 (2013).
8. Martínez-Franco, R. et al. Synthesis of an extra-large molecular sieve using proton sponges as organic structure-directing agents. *Proc. Natl Acad. Sci. USA* **110**, 3749–3754 (2013).
9. Jordá, J. L. et al. Synthesis of a novel zeolite through a pressure-induced reconstructive phase transition process. *Angew. Chem., Int Ed.* **52**, 10458–10462 (2013).
10. Eliášová, P. et al. The ADOR mechanism for the synthesis of new zeolites. *Chem. Soc. Rev.* **44**, 7177–7206 (2015).
11. Mazur, M. et al. Synthesis of 'unfeasible' zeolites. *Nat. Chem.* **8**, 58–62 (2016).
12. Kasneryk, V. et al. Expansion of the ADOR strategy for the synthesis of zeolites: the synthesis of IPC-12 from zeolite UOV. *Angew. Chem. Int Ed.* **56**, 4324–4327 (2017).
13. Firth, D. S. et al. Assembly–disassembly–organization–reassembly synthesis of zeolites based on cfi-type layers. *Chem. Mater.* **29**, 5605–5611 (2017).
14. Chlubná-Eliášová, P. et al. The assembly-disassembly-organization-reassembly mechanism for 3D-2D-3D transformation of germanosilicate IWW zeolite. *Angew. Chem. Int Ed.* **53**, 7042–7052 (2014).
15. Morris, S. A. et al. In situ solid-state NMR and XRD studies of the ADOR process and the unusual structure of zeolite IPC-6. *Nat. Chem.* **9**, 1012–1018 (2017).
16. Shamzhy, M. et al. Germanosilicate precursors of adorable zeolites obtained by disassembly of ITH, ITR, and IWR zeolites. *Chem. Mater.* **26**, 5789–5798 (2014).
17. Wheatley, P. S. et al. Zeolites with continuously tuneable porosity. *Angew. Chem., Int Ed.* **53**, 13210–13214 (2014).
18. Fritz, J. J. & Puget, C. R. Vapor pressure of aqueous hydrogen chloride solutions, 0° to 50° C. *Ind. Eng. Chem. Chem. Eng. Data* **1**, 10–12 (1956).
19. Laubengayer, A. W., Tabern, D. L. *J. Phys. Chem.* **30**, 1047–1048 https://doi.org/10.1021/j150266a005 (1925).
20. Trachta, M., Nachtigall, P. & Bludsky, O. The ADOR synthesis of new zeolites: in silico investigation. *Catal. Tod* **243**, 32–38 (2015).
21. Verheyen, E. et al. Design of zeolite by inverse sigma transformation. *Nat. Mater.* **11**, 1059–1064 (2012).
22. Corma, A., Rey, F., Valencia, S., Jorda, J. L. & Rius, J. A zeolite with interconnected 8-, 10- and 12-ring pores and its unique catalytic selectivity. *Nat. Mater.* **2**, 493–497 (2003).
23. Shvets, O. V., Kasian, N., Zukal, A., Pinkas, J. & Čejka, J. The role of template structure and synergism between inorganic and organic structure directing agents in the synthesis of UTL zeolite. *Chem. Mater.* **22**, 3482–3495 (2010).
24. Lorgouilloux, Y. et al. IM-17: a new zeolitic material, synthesis and structure elucidation from electron diffraction ADT data and Rietveld analysis. *RSC Adv.* **4**, 19440–19449 (2014).

Acknowledgements

M.S., M.M., R.E.M., J.Č. and M.O. acknowledge OP VVV "Excellent Research Teams" project No.CZ.02.1.01/0.0/0.0/15_003/0000417– CUCAM. M.S. and M.O. thank the Primus Research Program of the Charles University (project number PRIMUS/17/SCI/22 "Soluble zeolites"). R.E.M. also thanks the ERC (Advanced Grant 787073 "ADOR"). A.M. acknowledges The Centre for High-resolution Electron Microscopy (ChEM), supported by SPST of ShanghaiTech University under contract No. EM02161943, and the Natural National Science Foundation of China, through projects NFSC-21850410448 and NSFC-21835002. Z.L. acknowledges the support from the National Key Research and Development Program of China (2016YFA0300102) and the National Natural Science Foundation of China (11675179, 11434009). J.Č. acknowledges the support of the Czech Science Foundation to the project EXPRO (19-27551×).

Author contributions

V.K. and M.S. performed synthesis study and wrote respective sections of the article, Q.Y. performed lab-scale optimisation of the synthesis and basic characterisation of materials, A.M. and M.M. were responsible for microscopy and collecting of structural data, J.Z. and Z.L. designed and performed in situ experiments and respective analysis, R.E.M. and J.Č. analysed the results and supervised particular directions of the study, M.O. designed the synthesis strategy, analysed the results and wrote the article.

Competing interests

The authors declare no competing interests.

Additional information

Supplementary information is available for this paper at https://doi.org/10.1038/s41467-019-12882-3.

Correspondence and requests for materials should be addressed to Z.L. or M.O.

Peer review information *Nature Communications* thanks the anonymous reviewers for their contribution to the peer review of this work. Peer reviewer reports are available.

Reprints and permission information is available at http://www.nature.com/reprints

Publisher's note Springer Nature remains neutral with regard to jurisdictional claims in published maps and institutional affiliations.

Open Access This article is licensed under a Creative Commons Attribution 4.0 International License, which permits use, sharing, adaptation, distribution and reproduction in any medium or format, as long as you give appropriate credit to the original author(s) and the source, provide a link to the Creative Commons license, and indicate if changes were made. The images or other third party material in this article are included in the article's Creative Commons license, unless indicated otherwise in a credit line to the material. If material is not included in the article's Creative Commons license and your intended use is not permitted by statutory regulation or exceeds the permitted use, you will need to obtain permission directly from the copyright holder. To view a copy of this license, visit http://creativecommons.org/licenses/by/4.0/.

© The Author(s) 2019

Qiudi Yue

Email: qiudi.yue@natur.cuni.cz
ORCID: 0000-0003-2046-5238
Hlavova 8, Praha 2, Czechia

Education

PhD: Charles University (Czech Republic) 2017.10 – 2021.09
Physical Chemistry
Supervisor：Dr. Maksym Opanasenko Prof. Jiří Čejka

MSc: University of Science and Technology of China 2014.09 – 2017.07
Materials Chemistry
Supervisor：Prof. Pingwu Du

BE: Southwest Petroleum University (China) 2010.09 – 2014.06
New Energy Materials and Devices
Supervisor：Prof. Yuanpeng Wu Prof. Yun Huang

Research

Design, synthesis and characterization of new zeolite strcutures
Zeolite application in catalysis and gas separation
Synthesis of nanomaterials and their application in photo/electro-catalysis

Grant

1. Grant Agency of Charles University **PI** 2019 – 2021
Seeded growth of isomorphously substituted chabazites for separation of propylene/propane

2. National Undergraduate Training Programs for Innovation **PI** 2012 – 2013
Design and synthesis of magnetic nanomaterials as plugging agents

Publications

1. **Q. Yue**, K. Kutukova, E. Zschech*, A. Li, J. Čejka, M. Opanasenko*. Controllable zeolite AST crystallization mechanism: between the classical and reversed crystal growth. **Submitted.**

2. **Q. Yue**, J. Halamek, D. Rainer, J. Zhang, R. Bulánek, J. Čejka*, M. Opanasenko*. Tuning the CHA framework composition by isomorphous substitution for CO_2/CH_4 separation. **Submitted.**
3. **Q. Yue**, V. Kasneryk, M. Shamzhy, M. Mazur, Y. Zhou, P. Wheatley, R. E. Morris, J. Čejka, M. Opanasenko*. ADORable zeolite with 12×8×8-ring pores derived from IWR germanosilicate. **Submitted.**
4. **Q. Yue,** J. Zhang, M. Shamzhy, M. Opanasenko*. Seeded growth of isomorphously substituted chabazites in proton-form. **Microporous Mesoporous Mater.** 2019, 280, 331-336.
5. **Q. Yue**, C. Liu, Y. Wan, X. Wu, X. Zhang*, P. Du*. Defect engineering of mesoporous nickel ferrite for water oxidation Catalysis. **J. Catal.** 2018, 358, 1-7.
6. **Q. Yue**, Y. Wan, Z. Sun, X. Wu*, Y. Yuan, P. Du*. MoP is a Novel, Noble-metal-free cocatalyst for enhanced photocatalytic hydrogen production from water under visible light. **J. Mater. Chem. A** 2015, 3, 16941-16947.
7. J. Zhang, **Q. Yue,** M. Mazur, M. Opanasenko, M.V. Shamzhy*, J. Čejka. Selective recovery and recycling of germanium for the design of sustainable zeolite catalysts. **ACS Sustainable Chem. Eng.** 2020, 8, 8235-8246.
8. D. Jiang, **Q. Yue**, S. Tang, L. Zhang, L. Zhu, P. Du*. A highly efficient photoelectrochemical cell using cobalt phosphide-modified nanoporous hematite photoanode for solar-driven water splitting. **J. Catal.** 2018, 366, 275-281.
9. L. Zhu, **Q. Yue**, D. Jiang, H. Chen, R. M. Irfan, P. Du*. Metal-free graphene quantum dots photosensitizer coupled with nickel phosphide cocatalyst for enhanced photocatalytic hydrogen production in water under visible light. **Chin. J. Catal.** 2018, 39, 1753-1761.
10. Z. Sun, **Q. Yue**, J. Li, J. Xu, H. Zheng, P. Du*. Copper phosphide modified cadmium sulfide nanorods as a novel p-n heterojunction for highly efficient visible-light-driven hydrogen production in water. **J. Mater. Chem. A** 2015, 3, 10243-10247.
11. D. Jiang, L. Zhang, **Q. Yue**, T. Wang, Q. Huang, P. Du*. Efficient suppression of surface charge recombination by CoP-modified nanoporous $BiVO_4$ for photoelectrochemical water splitting. **Int. J. Hydrogen Energy** 2021, 46, 15517-15525.
12. Z. Sun, X. Liu, **Q. Yue**, H. Jia, P. Du*. Cadmium sulfide nanorods decorated with copper sulfide via one-step cation exchange approach for enhanced photocatalytic hydrogen evolution under visible light. **ChemCatChem** 2016, 8, 157-162.
13. M. Yang, Y. Huang*, **Q. Yue**, H. Cao, X. Li, Y. Lin. Preparation of a novel polymeric adsorbent and its adsorption of phenol in aqueous solution. **Desalin. Water Treat.** 2016,

57, 13295-13306.

14. R. M. Irfan, T. Wang, D. Jiang, **Q. Yue**, L. Zhang, H. Cao, Y. Pan, P. Du*. Homogeneous molecular iron catalysts for direct photocatalytic conversion of formic acid to syngas (CO+ H_2). **Angew. Chem. Int. Ed.** 2020, 59, 14818-14824.
15. V. Kasneryk, M. Shamzhy, J. Zhou, **Q. Yue**, M. Mazur, A. Mayoral, Z. Luo*, R. E. Morris, J. Čejka, Maksym Opanasenko*. Vapour-phase-transport rearrangement technique for the synthesis of new zeolites. **Nat. Commun.** 2019, 10, 1-8.

Conference

1. **Oral**：Department Seminar. “Labile extra-large pore elementosilicates as intermediates for design of novel catalysts”. Feb. 24, 2021, Prague, Czech Republic.
2. **Oral**: 8th Czech-Italian-Spanish Conference on Molecular Sieves and Catalysis. “Multiple phase transformations during the synthesis of germanosilicate UOS”, June 11-14, 2019, Amantea, Italy.
3. **Oral**: Department Seminar. “Seeded growth of isomorphously substituted chabazites and their potential application in gas separation”. Dec.12, 2018, Czech Republic.
4. **Poster**: Workshop on Low demensional Materials. “Between the classical and reversed crystal growth” Sep. 8-11, 2020. Liblice, Czech Republic.
5. **Poster**: Workshop on Layered Materials. “Multiple phase transformations during the synthesis of germanosilicate UOS”, Sep. 2-6, 2019, Chateau Liblice, Czech Republic.
6. **Poster**: XXII Forum Zeolitowe. "Design of zeolites of new structural types by intelligent reconstruction of germanosilicate frameworks“, June 19-23, 2018, Niepołomice, Poland.

Honors & Awards

- 2017 Excellent Graduate Student Award
- 2016 Suzhou Industrial Park Scholarship
- 2014 1st Undergraduate Thesis Award